nature chemistry

ARTICLES

https://doi.org/10.1038/s41557-018-0163-z

Visualizing pore architecture and molecular transport boundaries in catalyst bodies with fluorescent nanoprobes

Gareth T. Whiting*, Nikolaos Nikolopoulos, Ioannis Nikolopoulos, Abhishek Dutta Chowdhury and Bert M. Weckhuysen*

The performances of porous materials are closely related to the accessibility and interconnectivity of their porous domains. Visualizing pore architecture and its role on functionality—for example, mass transport—has been a challenge so far, and traditional bulk and often non-visual pore measurements have to suffice in most cases. Here, we present an integrated, facile fluorescence microscopy approach to visualize the pore accessibility and interconnectivity of industrial-grade catalyst bodies, and link it unequivocally with their catalytic performance. Fluorescent nanoprobes of various sizes were imaged and correlated with the molecular transport of fluorescent molecules formed during a separate catalytic reaction. A direct visual relationship between the pore architecture—which depends on the pore sizes and interconnectivity of the material selected—and molecular transport was established. This approach can be applied to other porous materials, and the insight gained may prove useful in the design of more efficient heterogeneous catalysts.

Porous materials are used on a global scale in a plethora of applications, from medicine to agriculture and the chemicals industry (among many others)[1–3]. The interplay between pore size, connectivity and accessibility impact materials' functionality on multiple length scales, from the molecular level through to the macroscopic level of behaviour[4–12]. A typical and yet important example is heterogeneous catalysis, which plays an enormous role in producing many of our everyday needs, such as materials, chemicals and fuels. Molecular transport to and from catalytic active sites via macro- (>50 nm), meso- (2–50 nm) and micro- (<2 nm) pores is a major factor in determining whether or not the catalyst is process efficient, consequently dictating its deactivation[13–16].

In an academic setting, the focus is normally on so-called 'research catalysts'[17], such as micro- and/or mesoporous fine powders or single crystals[18–21]. Although this develops the excellent and necessary fundamental knowledge, a more realistic example of an industrially applied heterogeneous catalyst is a shaped catalyst body containing catalytically active material (zeolite) dispersed in a matrix and/or binder (silica, alumina and/or clay)[17,22–28]. Such catalyst materials are imperative in a number of industrial processes (for example, hydrocarbon processing, which includes aromatization, alkylation and isomerization reactions[29–32]). These millimetre-sized catalyst bodies contain a complex hierarchical pore arrangement, from the macropores of the binder to (inter or intra) particle mesoporosity and zeolite micropores. The role of the binder component is essential for material strength, thermal stability, avoiding pressure drop and enhancing molecular transport. However, this last attribute depends on a high-level of meso- and macro-pore connectivity and accessibility in order that molecules can efficiently move into and out of the shaped bodies[32]. For instance, if these hierarchical pores are formed in such a way that a limited amount of interconnectivity is obtained, reactant molecules struggle to diffuse or navigate among the heterogeneous macro-, meso- and micropores, resulting in low product selectivities (due to sequential reaction mechanisms) and poor catalyst lifetime. Ideally, reactants should be free to navigate the well-connected hierarchical pore system (of the binder and zeolite components, both intra- and inter-particle space), before binding to a catalytic active site (for example, the Brønsted acid site in zeolite), reacting further with the desired product molecule(s) (that is, with other reactant and/or intermediate molecules), then leaving via the hierarchical pore network, eventually to the exterior of the catalyst particle.

So far, we have relied heavily on bulk and often non-visual measurements to obtain information, for example by probe molecule physisorption and/or porosimetry[33–35] (using Ar or Hg, respectively, which can be considered unrealistic for comparison with molecular access in some catalytic reactions) and/or diffusion measurements in large-scale materials[36]. Advances have been made to visualize the pore network in catalyst particles using advanced electron- and X-ray based techniques (such as focused ion beam–scanning electron microscopy (FIB–SEM) and transmission X-ray microscopy (TXM)), but these require elaborate studies with intricate sample preparation and/or synchrotron radiation[17,37–39]. In all cases, these approaches do not allow a facile and direct visual correlation between where and how interconnected and/or accessible these pores are and the effect this has on the material's actual functionality. Recently, a significant step was taken to spatially resolve catalytic events as well as the self-diffusion of realistically-sized molecules in single nanocatalysts[40] and fluid catalytic cracking (FCC) catalyst particles, respectively, using single-molecule fluorescence microscopy (SMF)[41,42]. However, linking pore architecture and performance in a visual manner, under realistic catalytic conditions, is yet to be accomplished.

Taking bio-imaging and petrographic imaging with fluorescent probes as inspiration (for example, in the former to discriminate between the size dependence of uptake and the transport of

Inorganic Chemistry and Catalysis group, Debye Institute for Nanomaterials Science, Utrecht University, Utrecht, The Netherlands. *e-mail: g.t.whiting@uu.nl; b.m.weckhuysen@uu.nl

fluorescent microspheres (representing regional blood flow) in lungs or other tissue[43–46], and in the latter to image void space in geomaterials[47,48]) we ask the question 'Can we establish a visual link between where specifically sized fluorescent probes are able to access and be taken up within a catalyst particle, and the molecular transport of fluorescent molecules within these regions during a catalytic reaction?' Developing this visual structure–function relationship of a catalyst (and other materials) will enable us to manufacture more efficient porous materials that, for instance, not only limit the production of waste, but also increase catalyst lifetime[49].

In this work we take an integrated, facile bio-imaging-inspired approach using fluorescent nanoprobes and confocal fluorescence microscopy (CFM) to resolve this knowledge gap. Two different clay-bound ZSM-5-based catalyst bodies (Z:Kaolin and Z:Bento) were impregnated with four specifically sized fluorescent nanoprobes (catalyst pore dimensions and typical feedstock-like molecules[41], ~2, 20, 45 and 100 nm in diameter), before imaging their uptake and correlating with the pore architecture and/or accessibility of meso- and macropores. The ~2 nm probe molecule was *N*,*N*′-bis(2,6-dimethylphenyl)-perylene-3,4,9,10-tetracarboxylic diimide (PDI), and the 20, 45 and 100 nm probes were all FluoSpheres carboxylate-modified microspheres. In a separate, yet integrated approach, a methanol-to-hydrocarbon (MTH) reaction was performed on corresponding fresh catalyst bodies. The fluorescent molecules, formed in a time-resolved manner during this reaction, were imaged within millimetre-sized catalyst bodies, and a clear, visual link was established between molecular transport, deactivation and accessibility during the zeolite-catalysed hydrocarbon conversion process.

Results and discussion

Linking pore architecture with catalyst deactivation using fluorescent nanoprobes. To determine the molecular diffusion and uptake properties, and hence accessibility parameters, of differently sized Z:Kaolin extrudates (1, 2 and 3 mm diameter), incubation time studies using a ~2 nm fluorescent nanoprobe were performed. Individual catalyst extrudates were impregnated with the probe, then removed at intervals (Fig. 1a) for bisectioning and CFM imaging to determine the probe penetration depth and corresponding probe uptake (in $\mu m\,min^{-1}$). From the uptake profile of the largest Z:Kaolin (3 mm diameter) extrudate it is evident that at least three diffusion regimes (R1, R2 and R3) exist, with the probe penetrating quickly to a depth of 220 ± 22 μm (R1) at a rate of 15 $\mu m\,min^{-1}$, before slowing to a rate of 0.6 $\mu m\,min^{-1}$ (R2) and then to 0.06 $\mu m\,min^{-1}$ (R3). A visual representation of this uptake process is provided in Fig. 1a, where the CFM images were taken at specific time intervals, and again reveal a substantial uptake of the ~2 nm probe in the first 240 min (358 ± 9 μm), before abating (434 ± 49 μm after 1,440 min (24 h)). Although the probe appears to come to a halt at an 'ideal' boundary (Fig. 1a), higher magnification (Supplementary Fig. 1) reveals that the probe fades away immediately after this 'boundary', suggesting pore narrowing. However, considering that the majority of the probe slows to such a definitive depth, we will refer to it as a boundary throughout.

A similar uptake profile is observed for the 2-mm-diameter Z:Kaolin extrudates (Fig. 1a), but slightly slower uptake rates are obtained in the first two regions (13 $\mu m\,min^{-1}$ in R1 and 0.4 $\mu m\,min^{-1}$ in R2) compared to those of the 3-mm-diameter Z:Kaolin. However, the uptake profile of the 1-mm-diameter extrudate (Fig. 1a) differs significantly from those of the 2- and 3-mm-diameter extrudates, where in R1, almost double the rate of probe uptake is obtained (28 $\mu m\,min^{-1}$) compared to the other two extrudates (13 and 15 $\mu m\,min^{-1}$, respectively). Although the rate of uptake in the 1-mm-diameter Z:Kaolin in R2 is similar to that of the larger extrudates (0.4 $\mu m\,min^{-1}$), the probe has already reached a depth of 420 ± 10 μm in R1, which is 84% of its potential maximum uptake. Considering the penetration depths observed after 24 h (1,440 min) incubation in 2- and 3-mm-diameter Z:Kaolin (408 ± 54 and 434 ± 49 μm, respectively), it is highly plausible that, due to the smaller size of the 1 mm extrudate, the calcination treatment is able to draw out water and organics (used during extrudate preparation) more homogeneously from the pores in the smaller extrudate compared to the larger extrudates, creating a more accessible uniform and/or well-connected pore system.

As a proof of concept that calcination treatment plays such a considerable role in determining pore architecture and/or accessibility, 2-mm-diameter Z:Kaolin extrudates were prepared and calcined at 500, 550 and 600 °C (Supplementary Fig. 2). Uptake profiles and CFM images at certain incubation time intervals reveal a trend in accessibility as follows: Z:Kaolin(500) > Z:Kaolin(550) > Z:Kaolin(600). This matches the trend in pore volumes measured by Hg porosimetry analysis (Supplementary Fig. 2), which can be explained by the dehydroxylation of the kaolinite binder phase to metakaolin under higher calcination temperatures (this has a denser structure than kaolinite[50]).

To investigate accessibility into pores of varying dimensions and their degree of interconnectivity in Z:Kaolin extrudates, we used 20, 45 and 100 nm fluorescent nanoprobes that are of similar dimensions to the available pores (Supplementary Fig. 3). By impregnating the Z:Kaolin extrudates with any one of the fluorescent nanoprobes, followed by 24 h incubation, bisectioning and 3D CFM imaging, a visual relationship between the size of the probe and its accessibility into the catalyst bodies is established.

By marking the transport limitation regions (R1–R3) from Fig. 1a on the penetration depth charts for these larger nanoprobes (Fig. 1b), a link between their behaviour and pore accessibility is evident. First, taking the largest nanoprobe (100 nm in diameter), it is clear that although Hg porosimetry revealed macropores in the range of 100–600 nm (Supplementary Fig. 3), they are actually difficult to access from the external surface, with minimal penetration observed (<12 μm) (Fig. 1b). Staining with 45 nm nanoprobes displayed penetration depths of 127 ± 37, 164 ± 58 and 195 ± 54 μm in 1-, 2- and 3-mm-diameter Z:Kaolin extrudates, respectively (Fig. 1b and Supplementary Fig. 4), with impregnation of the 20 nm probe showing depths of 362 ± 123, 228 ± 50 and 254 ± 26 μm (1-, 2- and 3-mm-diameter Z:Kaolin extrudates, respectively). A surprising feature of the 2- and 3-mm-diameter Z:Kaolin extrudates impregnated with 20 and 45 nm probes is that both probes curtail at (or near to) the interface of R1 and R2 (192 ± 7 and 220 ± 22 μm, respectively). This provides substantial evidence for pore architectural size differences throughout the cylindrical extrudates, most probably due to a radial gradient of pore narrowing from the extrudate exterior to its interior. In the case of the 1-mm-diameter Z:Kaolin extrudate, the 20 nm probe also curtails close to the interface of R1 and R2 (420 ± 10 μm), but the 45 nm probe stops at a depth well before (127 ± 37 μm). Given the similarity in uptake behaviour of the ~2 nm and 20 nm probes (compared to the 45 nm probe), this backs our previous theory that more uniform (but narrower) pores are formed upon calcination in the smallest extrudate, compared to its larger counterparts.

Given the significance of these findings (specifically, the different uptake regimes and more homogeneous pores in the 1-mm-diameter Z:Kaolin), it is essential to understand how such accessibility parameters relate to the functionality and deactivation profiles of these catalytic materials. MTH is a global zeolite-catalysed reaction for converting methanol into larger, more valuable chemical building blocks, such as ethylene and propylene (important to the polymer industry)[51,52]. Larger aromatic molecules are also formed that can be valuable (*para*-xylene), but these molecules can oligomerize to produce even larger polyaromatic molecules that eventually cause catalyst deactivation (for example, pore blockage). Therefore, due to the production and transport of differently sized molecules within the catalyst bodies, MTH is an excellent means

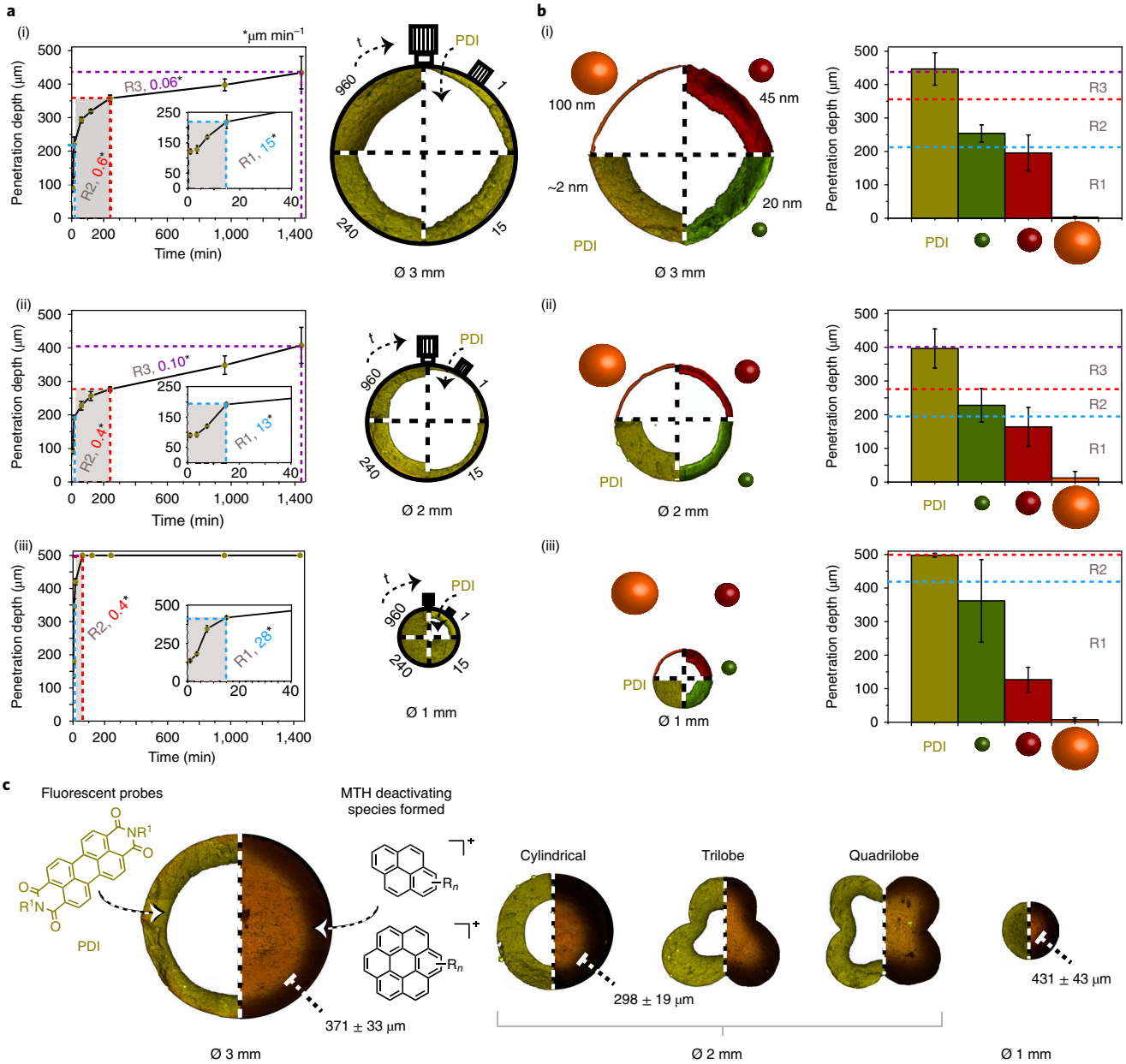

Fig. 1 | Visualizing accessibility and deactivation in zeolite-based catalyst bodies. a, Incubation time uptake measurements of a ~2 nm fluorescent nanoprobe in Z:Kaolin extrudates with (i) 3 mm diameter (Ø); (ii) 2 mm diameter; (iii) 1 mm diameter. Left, Penetration depth measurement versus time profiles, with different molecular transport rate regimes or regions (R1–R3) highlighted. R1: 0–15 min, up to the light blue dotted line; R2: 15–240 min, from the light blue dotted line to the red dotted line; R3: 240–1,440 min, from the red dotted line to the purple dotted line. Right, 3D CFM images of Z:Kaolin quadrants from selected incubation time intervals, providing a visual representation of the fluorescent probe uptake (slowing over time) in each case. Error bars are based on s.d. of six penetration measurements from two extrudates (Supplementary Table 2). **b**, 24 h incubation with differently sized fluorescent nanoprobes in Z:Kaolin extrudates with (i) 3 mm diameter; (ii) 2 mm diameter; (iii) 1 mm diameter cross-sections. Left, Top-view 3D CFM images of the penetration of four specifically sized fluorescent nanoprobes in quadrants (see Supplementary Fig. 4 for full cross-sections). Error bars are based on s.d. of 12 penetration measurements from three extrudates (Supplementary Table 3). Right, Corresponding charts revealing the quantitative penetration depth measurements of each nanoprobe. Transport regions (R1, R2 and R3 from the incubation time studies, **a**) are highlighted to show how they impact the penetration depth of the differently sized nanoprobes. **c**, 'Half-half' images of differently sized Z:Kaolin extrudates impregnated with a ~2 nm nanoprobe (24 h incubation) (left half) and 3D top-view CFM images (using 488 and 642 nm lasers simultaneously) of methanol-to-hydrocarbon (MTH) reacted Z:Kaolin extrudates, removed from the reactor (and bisected and imaged) after 75 min of reaction time (right half). Black, non-fluorescent regions are coke species; orange fluorescence in the core is related to a mixture of both large and small (more and less conjugated, respectively) species. Depth measurements were taken from the outside of the extrudate to where the orange fluorescent region starts (shown by a blunt-headed arrow), revealing a similarity in the depth at which the ~2 nm probe uptake slows (**a**,**b**). MTH deactivating species refers to large polyaromatic molecules, as exemplified by pyrene and coronene molecules, formed via oligomerization reactions, which block pores within the catalyst body.

to investigate the relationships between pore architecture, molecular transport and catalyst deactivation. By performing the MTH reaction in a fixed-bed reactor loaded with Z:Kaolin extrudates, and subsequently removing them after a period of reaction time, 3D CFM can be used to explore the extent of coking within the catalyst bodies[53]. Moreover, ZSM-5 within the Z:Kaolin extrudates

conveniently catalyses the formation of light absorbing species (carbocations) that can be excited with specific wavelength lasers, akin to the absorption maxima of such species[54]. On removal of the extrudates from the reactor, bisectioning and then imaging with 488 and 642 nm lasers simultaneously, the location of both large (more conjugated) and small (less conjugated) species, respectively, can be visualized (the higher the degree of conjugation, the longer the absorption wavelength[55]) (Supplementary Methods).

Figure 1c presents 'half–half' CFM top-view 3D images of 1-, 2- and 3-mm-diameter Z:Kaolin extrudates after (left half) 24 h incubation of a ~2 nm probe and (right half) 75 min of MTH reaction. It is evident that a boundary exists, with the latter producing a non-fluorescent zone around the near-edge region of the cross-section, with a fluorescent orange core. The non-fluorescent zone is attributed to large polyaromatic species, such as graphitic coke molecules[54] (akin to the size of the ~2 nm probe), whereas orange fluorescence in this case is typical of a mixture of less and more conjugated species (that is alkylated naphthalene and pyrene carbocations, respectively). More notably, the depth at which the non-fluorescent coke regions are found inside the MTH reacted catalyst bodies lies around the interface of R2 and R3 (and R1 and R2 for the 1-mm-diameter extrudate), as highlighted in Fig. 1b. The similarity in the depth of the coke region with that of the second uptake limitation in the ~2 nm probe incubation experiments points towards a link between pore narrowing and limited molecular transport, leading to the formation of coke precursors and, eventually, catalyst deactivation.

As a proof of concept, this also appears to be the case when using differently shaped extrudates (Fig. 1c). For instance, using tri- and quadrilobe extrudates, a very similar non-fluorescent coke region replicates near perfectly the region penetrated by the fluorescent nanoprobes for these shaped materials (Supplementary Fig. 5), revealing that the shape of the extrudate is independent of the pore architecture.

Micro-spectroscopic revelations of molecular transport boundaries. Given that a specific region of the catalyst extrudate is influential in forming coke molecules after 75 min of MTH reaction, it is then interesting to observe how such molecular transport boundaries impact earlier stages of the MTH reaction. Using a similar approach, Z:Kaolin extrudates were removed after 15 min reaction time, before bisectioning. Optical absorption spectra were subsequently measured at the core and near-edge regions (similar to those regions that are inaccessible and accessible to the nanoprobes, respectively) within each cross-section. Due to the broad nature of the commonly reported visible absorption bands produced during MTH[55–57], it is highly unlikely that only one type of molecule is excited when using specific laser line wavelengths (Fig. 2a). However, using both short- and long-wavelength lasers simultaneously (488 and 642 nm, respectively) ensures limited spectral overlap, and a relative discrimination between the location of 'small or less conjugated' (alkylated benzenes and/or naphthalenes (N): green fluorescence) and 'large or more conjugated' (alkylated phenanthracenes (PH), pyrenes (PY) and/or (LPAs): red fluorescence) species.

From Fig. 2b (Supplementary Fig. 6), it is clear that even at this early stage of the reaction a similar molecular transport boundary, akin to that inaccessible to the fluorescent nanoprobes, exists. A combination of small (less conjugated) and larger (more conjugated) species (orange fluorescence) are located in the core of the cross-section (Fig. 2c), with a high concentration of mainly smaller species (green fluorescence) located at the near-edge region[55–57]. As with the coke region observed after 75 min of MTH in Fig. 1c, the dimensions of this near-edge region of green fluorescence after 15 min match closely that accessible to the nanoprobes, revealing a consistency of the accessibility measurements and molecular transport in porous media. Furthermore, it appears that the smallest extrudate size (1 mm diameter) allows the formation of larger species in general (Fig. 2c), with a more homogeneous distribution of orange fluorescence throughout the cross-section, again corroborating the high accessibility observed in fluorescent nanoprobe uptake studies (Fig. 1). This relation between extrudate diameter, pore architecture and the link to molecular transport should be a crucial factor when selecting extrudates of a specific size, and not just for pressure drop concerns.

Interestingly, if we look at Z:Kaolin cross-sections at reaction time periods before and after 15 min (Fig. 3 and Supplementary Fig. 6), detailed mechanistic insights into molecular transport during MTH can also be observed. After 2 min of reaction, again, a similar boundary separating two different types and/or sizes of molecule exists; however, here, a red fluorescent near-edge region exists together with a fluorescent green core, which is in stark contrast to that observed after 15 min. Given the visual confirmation of the accessibility of the nanoprobes into this very specific region and their inaccessibility further into the core (Fig. 1a,b), this inaccessible boundary (most probably due to pore narrowing and/or disconnected pore networks) clearly creates a limitation in molecular transport towards the core. Oligomerization to form larger molecules ensues (PH and PY) at the near-edge, leaving a substantial core of smaller molecules (B and N) (Supplementary Fig. 7).

Because these larger pyrene-type molecules occupy the perimeter of the extrudate, smaller molecules at the core have difficulty leaving via the once accessible near-edge region, leading to oligomerization to larger molecules within the core of the extrudate over time, hence the orange fluorescence after 15 min. At the same time, pyrene-type molecules contained in the near-edge region are less likely to leave the extrudate, given their large dimensions, and therefore undergo cracking reactions, leading to the formation of smaller benzene and naphthalene molecules in this region (hence green fluorescence at 15 min). Online gas chromatography (GC) analysis of products leaving the reactor bed provide evidence of cracking reactions (Fig. 3d). It is clear that at 2 min of reaction, a lower yield ratio of C_5 olefins to C_3 olefins is produced due to blocking of pores by the pyrene-type molecules around the near-edge region. However, after 15 min, there is a significantly higher formation of C_5 oligomers leaving the Z:Kaolin extrudates, which are most probably formed from the cracking of these larger aromatic molecules.

At 30 min of MTH reaction, it is clear that deactivation has started to take place, with the near-edge region containing more non-fluorescent species such as graphitic coke molecules, which again trap the movement of species out of the core. This deactivation then continues at 75 min of reaction (via oligomerization with methanol and/or intramolecular transformations), with the higher concentration of coke species at the perimeter blocking pores, leading to a decreasing yield of C_5 olefins compared to smaller C_3 olefins (Fig. 3d).

Effect of changing pore architecture on accessibility and performance. This revelation into the visual relationship between pore architecture and performance is crucial to understanding how to make more efficient catalyst bodies, but so far only one specific porous medium (Z:Kaolin) has been studied. The question remains—can this bio-inspired approach also be applied to investigate the effect of using different porous media on the performance?

To unequivocally determine the effect of accessibility in catalyst materials, 2-mm-diameter Z:Kaolin(500) (calcined at 500 °C) and 2-mm-diameter Z:Bento (bentonite binder instead of kaolinite) were selected due to their considerable difference in pore volume, as shown by Hg porosimetry analysis (Supplementary Fig. 8). Nanoprobe (~2 nm) incubation time accessibility studies (Fig. 4a) support pore volume measurements with vastly different uptake profiles. For example, in R1, Z:Kaolin(500) shows an uptake rate of 40 μm min^{-1} (depth of 606 ± 7 μm), compared to 5 μm min^{-1}

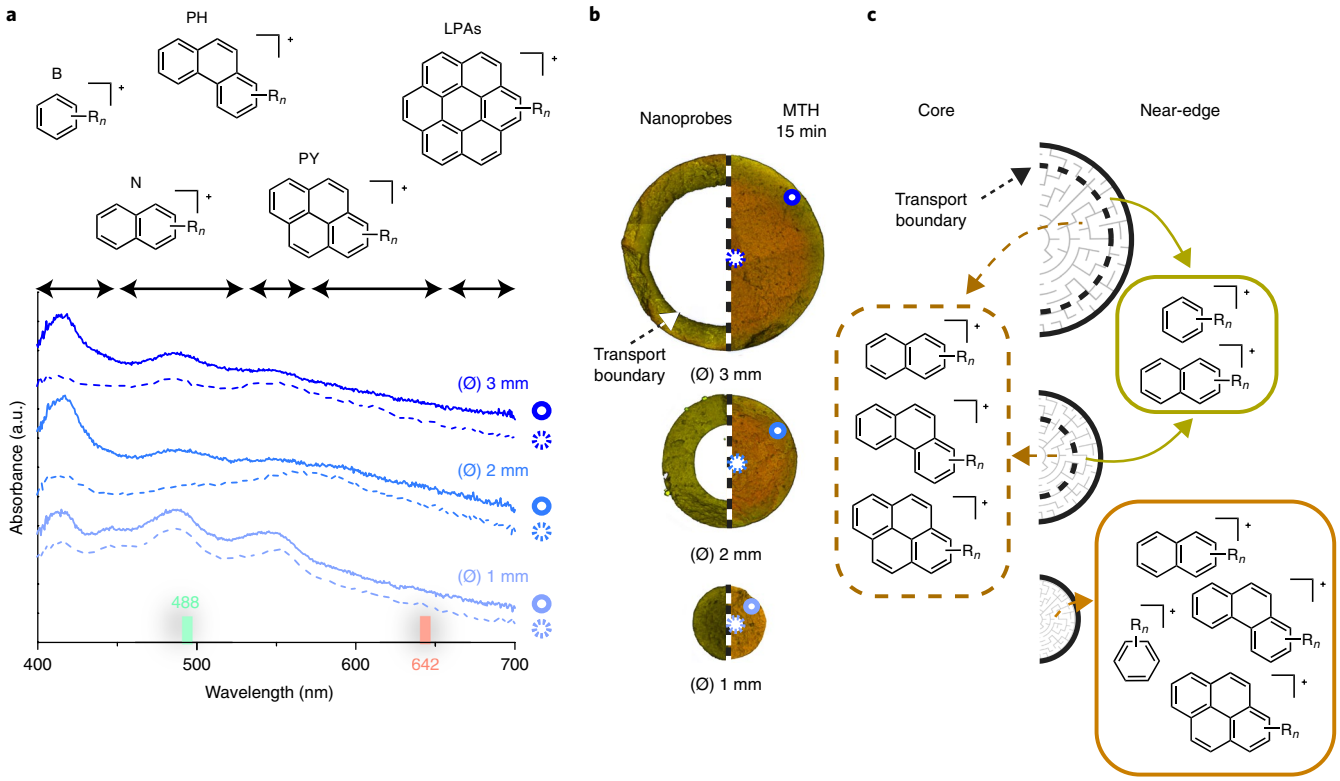

Fig. 2 | Associating molecule size, type and location with accessibility. a, Visible absorption spectra of Z:Kaolin (3, 2 and 1 mm diameter) taken from the MTH reactor after 15 min, and spectra spot checking at the near-edge region (full circle) and core (dotted circle) of the extrudate cross-sections. Typical molecules found in the visible region of the spectra are indicated, with larger or more conjugated species found on the right-hand side of the spectrum and smaller or less conjugated species located on the left-hand side of the spectrum. **b**, Half-half 3D top-view CFM images of Z:Kaolin extrudate cross-sections after ~2 nm fluorescent nanoprobe impregnation (left half) and after 15 min of MTH reaction, excited using 488 and 642 nm lasers simultaneously (right half). Positions of the corresponding optical spectra in **a** are also depicted (by full and dotted circles). **c**, Schematic representations of the type and location and/or distribution of molecules observed within the differently sized extrudates. The similarity between the position of the transport boundary witnessed in the fluorescent nanoprobe experiments (**b**) and the corresponding molecular transport boundary observed in the MTH reacted samples is clear and significant.

(depth of 69 ± 3 μm) achieved by Z:Bento. The probe penetration abates in R2 (as in previous studies; Fig. 1a), with an uptake rate of 0.4 μm min^{-1} for Z:Bento and 1.7 μm min^{-1} for Z:Kaolin(500) (the latter reaches its maximum (1,000 μm) penetration depth during this regime). When removing each extrudate from the MTH reactor after 15 min and chemically mapping the species within each cross-section (Fig. 4b), there is a striking difference between the types and locations of the species present. As expected, due to the highly accessible nature of the pores in Z:Kaolin(500), a homogeneous orange fluorescence is observed throughout the cross-section, which matches well the penetration depth of the ~2 nm probe after 24 h incubation. The orange fluorescence is attributed to a mixture of small and large species (Fig. 4c,d), which indicates an efficient molecular transport system. On the other hand, Z:Bento displays a shallow green fluorescent zone of mainly smaller species at the near-edge region of the extrudate, which closely matches that accessible to the ~2 nm probe. A deep red fluorescence within the sizable core of the reacted Z:Bento is attributed to larger alkylated pyrene molecules (Fig. 4c,d). With this clear distinction in location between small and large molecules, it is unequivocally clear that pore narrowing is causing larger molecules to become trapped in the core of the extrudate, once they are formed.

Analysis of the yield ratio of larger C_5 olefins to smaller C_3 olefins confirmed that, indeed, larger molecules are able to leave Z:Kaolin(500) more efficiently than Z:Bento (Fig. 4e).

To understand the decreasing trend in C_5:C_3 olefins over time, both 2-mm-diameter Z:Kaolin(500) and Z:Bento extrudates were investigated after 2, 15, 30 and 75 min of MTH reaction (Fig. 4e, inset images). After 2 min, Z:Kaolin(500) displays a homogeneous orange fluorescence throughout, whereas Z:Bento displays a smaller red fluorescent near-edge region, with a substantial green fluorescent core. This shallower outer region of accessibility in Z:Bento, coupled with the formation of larger pyrene-type (PY) molecules located therein, appears to be trapping smaller molecules within the core of the extrudate, preventing molecules such as C_5 olefins from leaving. This can be observed by the substantially lower yield ratio of C_5:C_3 olefins for Z:Bento, compared to the more accessible Z:Kaolin(500) at 2 min reaction time.

As the reaction proceeds, limited molecular transport from the core to the exterior of the extrudates leads to deactivation in both cases (more so in the case of Z:Bento). At 30 min of reaction time, oligomerization of alkylated benzene and naphthalene (B and N) molecules to larger polyaromatic species in both samples leads to the formation of graphitic coke-like molecules (non-fluorescent coronene). Such coke molecules block access into and out of the catalyst bodies, contributing to a 'coking front' that is observed to move towards the core of the extrudates over time, leading to catalyst deactivation.

This study shows us that, for heterogeneous catalyst bodies, we should be aware that when attempting to tailor their degree of

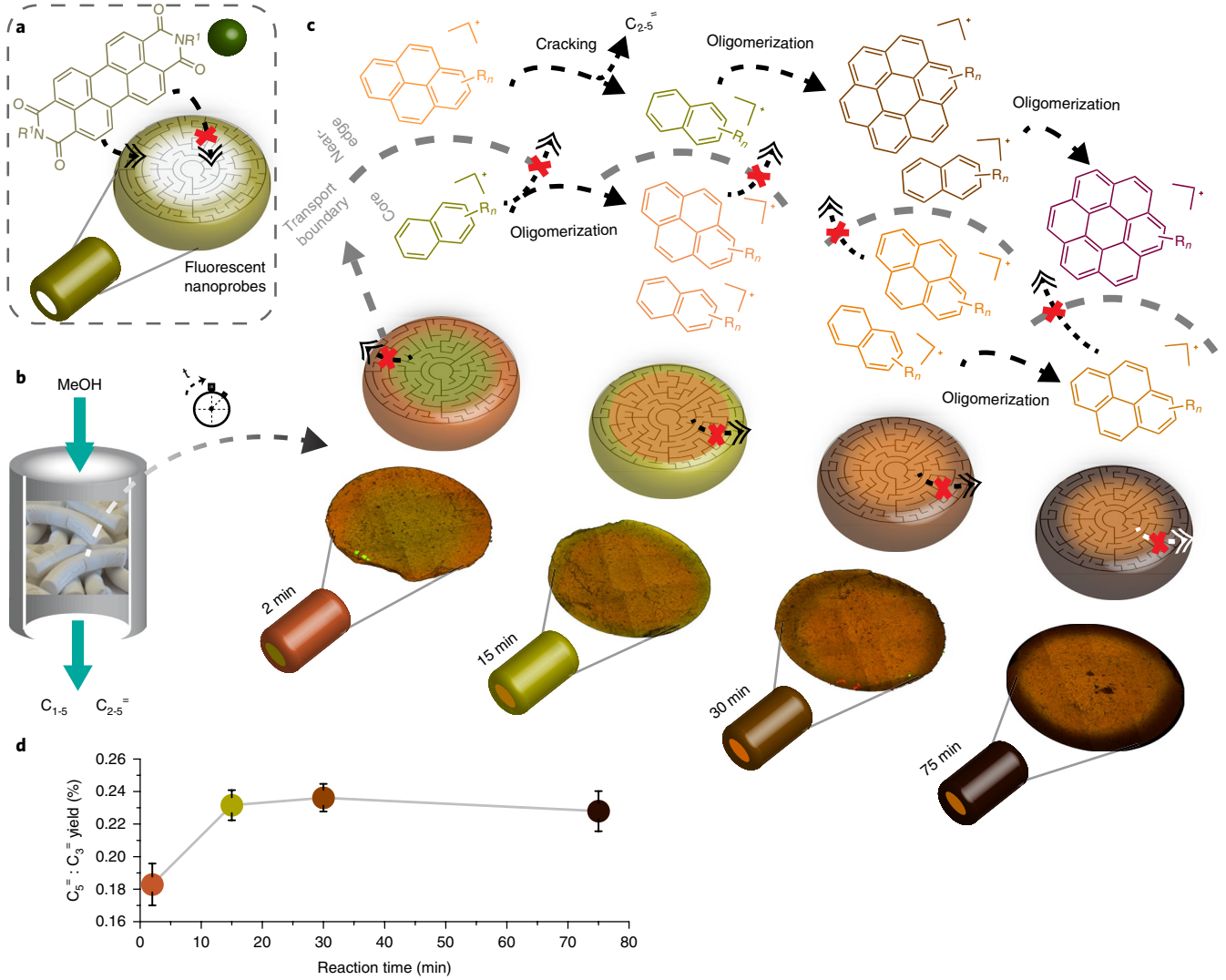

Fig. 3 | Visualizing molecular transport phenomena at different stages of a MTH reaction. a, Schematic key representation of the penetration depth and transport boundary observed by ~2 nm and 20 nm fluorescent nanoprobe (shown as a molecular structure and green sphere, respectively) accessibility studies on the 3 mm diameter Z:Kaolin catalyst bodies (Fig. 1a,b). **b**, Schematic representation of the reactor. C2-5$^{=}$ represent C2-5 olefins. **c**, 3D top-view CFM images (after simultaneous excitation with 488 and 642 nm lasers) after removal from the reactor (and bisectioning) at different MTH reaction times. Fluorescence colours in each CFM image are attributed to the types of molecule located within the different regions of accessibility within the extrudate (Supplementary Methods). Schematic representations of each CFM cross-sectional image are provided directly above, showing the effect of the molecular transport boundary on the mechanistic pathways that exist during the MTH reaction. Optical absorption spectra (Supplementary Fig. 7) taken at the 'near-edge' and 'core' regions gave rise to the molecules, whose structures are displayed with colour coding of the molecules linked to the fluorescence colour in the CFM images below (to further highlight their location within the extrudate). It is evident that as the MTH reaction proceeds, the molecules in each region undergo either cracking or oligomerization mechanisms to form other fluorescent products (hence the fluorescence colour changes over time in the two specific regions of accessibility). **d**, Online gas chromatography analysis of product molecules able to leave the reactor containing 3-mm-diameter Z:Kaolin—specifically, the ratio between C_5 olefins and C_3 olefins—over time. Error bars are based on the s.d. of three separate experiments (Supplementary Table 3).

accessibility, there is a fine balance between the pore dimensions and/or interconnectivity, the types of molecules produced therein, their transport, and deactivation of the catalyst.

Conclusions

We report a direct visual representation linking pore architecture with molecular transport and performance, under realistic catalytic conditions in porous catalyst bodies. By correlating fluorescent nanoprobe pore accessibility imaging with the location and type of fluorescent molecules formed during a separate catalytic reaction, a direct visual relationship between the degree of accessibility and/or interconnectivity and its effect on molecular transport has been established. Dependent on the size of the catalyst body and the choice of porous binder, variations in probe accessibility were observed to unequivocally impact the functionality of the catalysts during a separate MTH reaction study. In particular, the region of accessibility probed in each sample significantly dictated the size and/or type and location and/or transport of molecules formed, hence dictating deactivation. A larger region of accessibility increased the amount of larger products able to leave the catalyst bodies; however, at their own expense, larger polyaromatics were allowed to form over time, leading to deactivation. Compared to traditional bulk pore measurements, this enhanced integrated imaging approach into the link between pore architecture and

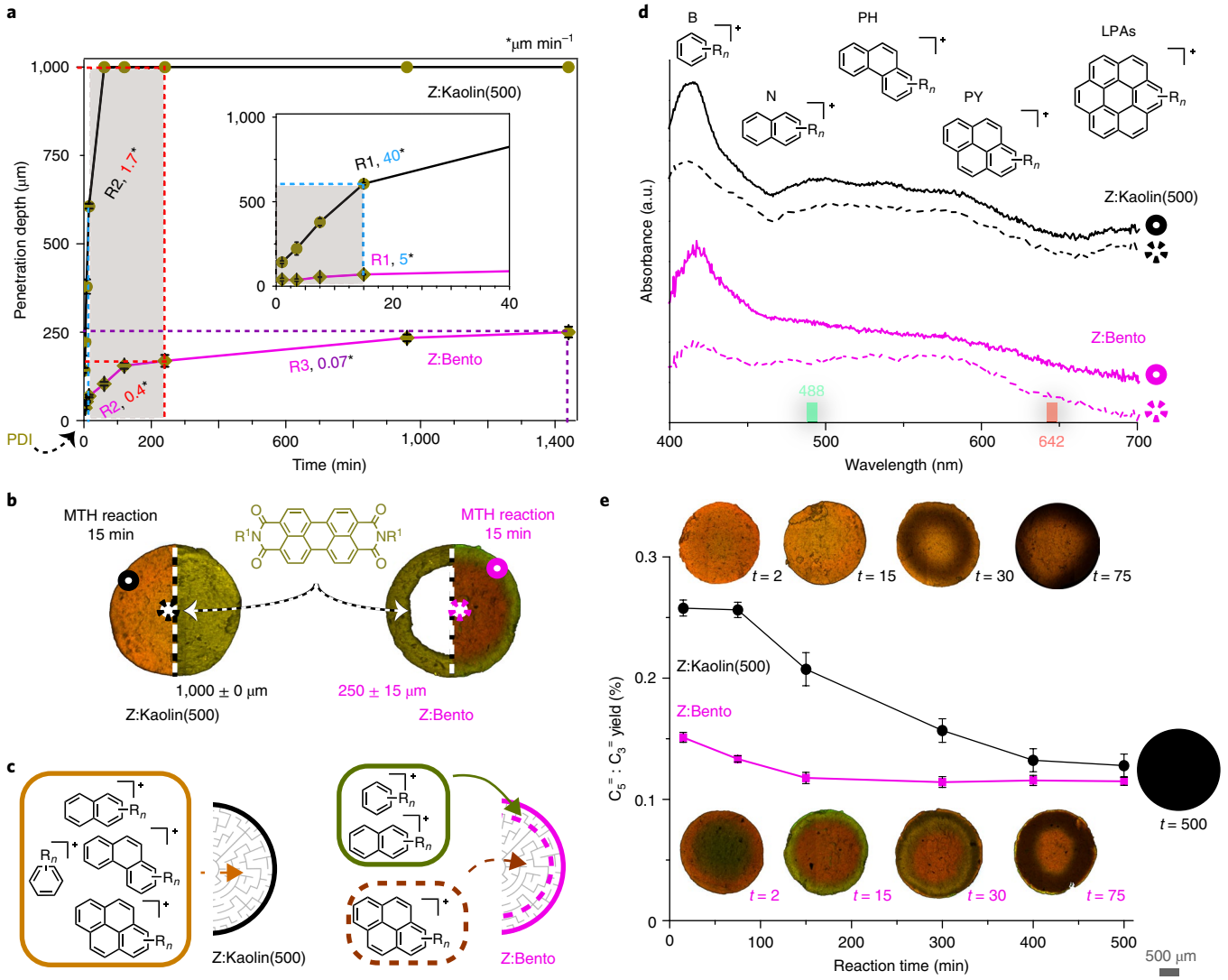

Fig. 4 | Visualizing the effect of changing accessibility on catalyst performance. a, Incubation time uptake measurements of ~2 nm fluorescent nanoprobes in Z:Kaolin(500) (solid black line) and Z:Bento (solid magenta line) 2 mm diameter extrudates, with different molecular transport rate regimes highlighted (R1–R3). R1: 0–15 min, up to the light blue dotted line; R2: 15–240 min, light blue dotted line to the red dotted line; R3: 240–1,440 min, up to purple dotted line, only shown for Z:Bento. Error bars are based on the s.d. of six penetration measurements from two extrudates (Supplementary Table 2). **b**, Half-half CFM images of 2-mm-diameter Z:Kaolin(500) (left) and Z:Bento (right) after ~2 nm fluorescent nanoprobe incubation for 24 h and after 15 min of MTH reaction (left half and right half, respectively). **c**,**d**, Schematic representations of the type and location or distribution of molecules observed within both extrudates after 15 min of MTH reaction (**c**) as measured by optical absorption spectra (**d**) taken at the near-edge (solid circle, **b**) and core regions (inside dotted circle, **b**) of both Z:Kaolin(500) (black) and Z:Bento (magenta) MTH reacted cross-sections, with the related molecules expected at each region of the spectra depicted. **e**, Ratio of the yield of C_5 to C_3 olefins that are able to leave 2-mm-diameter Z:Kaolin(500) and Z:Bento after different stages of the MTH reaction (measured in operando using an online GC). CFM images of full extrudate cross-sections after 2, 15, 30 and 75 min (t) of reaction are shown as insets, demonstrating the effect on the types of molecules present and their specific location based on the substantial difference in accessibility between the two catalysts as observed in **a**. Error bars are based on s.d. of three separate experiments (Supplementary Table 4).

performance in porous catalyst bodies can lead to the manufacture of enhanced materials, whereby regions of accessibility can be tailored to influence product formation and/or deactivation. Not only can this facile bio-inspired approach of fluorescent nanoprobes be used to study alternative porous media within the field of catalysis, but it can also be applied to study an even wider range of important meso- and macro-porous materials, such as controlled drug delivery carriers, membranes, batteries and biomaterials.

Methods

Shaped catalyst body preparation. Zeolite H-ZSM-5 (ACS Materials, M38) was mixed as a dry powder with either kaolinite (Sigma Aldrich, Natural) or bentonite (SWy-3, Source Clays Repository, The Clay Minerals Society), methylcellulose (Sigma Aldrich, 4,000 cP) and the required amount of Milli-Q water to ensure an optimum solid-to-liquid ratio for extrusion (measured using a mixer torque rheometer, Caleva). The paste, containing a ratio of 70:30 wt% zeolite:binder, was extruded using a Mini-Screw Extruder (Caleva) through a 1-, 2- or 3-mm-diameter die plate of either cylindrical, trilobe or quadrilobe shape. After drying overnight, the extrudates were calcined in a tubular furnace at 823 K for 6 h (5 K min^{-1}) in flowing air. Kaolinite-bound ZSM-5 extrudates are termed Z:Kaolin, whereas bentonite-bound ZSM-5 extrudates are termed Z:Bento. In the case of Z:Kaolin extrudates, assume a calcination temperature of 550 °C unless stated otherwise (that is, Z:Kaolin(500) is calcined at 500 °C).

Physicochemical characterization. Ar physisorption of the catalyst bodies was performed using a Micromeritics TriStar 3000 instrument. Before the

measurements, the samples were outgassed for 16 h at 300 °C under a dry N_2 flow, with measurements performed using Ar at −196 °C. Hg porosimetry measurements were carried out in a Poremaster (Quantachrome) instrument. The extrudates were degassed in a N_2 flow at 80 °C overnight. Surface tension (γ) and contact angle (θ) were set to 485 dyn cm^{-1} and 130°, respectively, and the materials infiltrated in the pressure range $p = 2 \times 10^{-2} - 55{,}000$ psi, to probe pores with a minimal diameter of 6 nm. The sample were subjected to two intrusion–extrusion cycles, and the Washburn law $p = -4\gamma\cos\theta/d$ was applied in the pressure range probed. SEM was performed using an FEI Helios Nanolab G3 instrument, and before analysis the extrudate cross-sections were coated with a layer of Pt to increase the conductivity of the samples. Powder X-ray diffraction (PXRD) patterns of the catalyst bodies (crushed and flattened) were recorded on a Bruker D8 X-ray powder diffractometer equipped with a Co Kα X-ray tube ($\lambda = 1.7902$ Å). Temperature-programmed desorption of ammonia (NH_3-TPD) was performed using a Micromeritics AutoChemII 2920 equipped with a TCD detector. Catalyst (0.1 g) was first outgassed in He for 1 h at 600 °C with a heating ramp of 10 °C min^{-1}. Ammonia was adsorbed at 100 °C until saturation using a flow of 25 ml min^{-1} of 10% NH_3 in He, followed by flushing with He for 120 min at 100 °C. Ammonia desorption was monitored using the TCD detector until 600 °C, with a ramp of 10 °C min^{-1}. FIB–SEM images were recorded on an FEI Helios NanoLab G3 UC (FEI Company) instrument in a similar manner to routine FIB–SEM measurements described in the literature[58]. A protective layer of Pt was deposited on top of the region of interest, before milling trenches either side. Slices were milled perpendicular to the surface, before SEM images were recorded in backscatter mode (2 kV, 50 pA).

Staining and visualization. The ~2 nm probe molecule, *N*,*N*′-bis(2,6-dimethylphenyl)-perylene-3,4,9,10-tetracarboxylic diimide (**PDI**, Sigma Aldrich) is a highly fluorescent and photostable dye with an absorption maximum at 525 nm. The probe molecule was diluted to 1.67×10^{-4} M in toluene and impregnated in single catalyst bodies for nine different time periods (1, 3.5, 7.5, 15, 60, 120, 240, 960 and 1,440 min), before removal, drying under atmospheric conditions, bisectioning and imaging with a 488 nm laser. Larger probes of 20, 45 and 100 nm (FluoSpheres, carboxylate-modified microspheres in Milli-Q water, ThermoFisher Scientific) were also impregnated in similar experiments (for a period of 24 h incubation), and imaging with 488, 642 and 561 nm lasers, respectively. Imaging was performed using a confocal fluorescence Nikon Eclipse 90i microscope equipped with a pin hole to filter out-of-focus light, and dichroic mirrors corresponding to the relevant laser line wavelength were used. The microscope was equipped with a Nikon A1 scan head, accommodating the optics, which coupled fibre optics for excitation and emission light with the microscope. A Nikon ×10/0.30 objective was used along with a spectral analyser in the Nikon A1 system, equipped with 32 photomultiplier tubes (PMTs) set to collect emission light in the region of 487–720 nm (resolution of 10 nm). 3D reconstruction of the individual imaged slices produced volumes of 1.29 × 1.29 × ~0.5 mm (x, y, z (depth), respectively), visualized as top-view images. Probe penetration depths were measured manually using the microscope software, and were evaluated for two catalyst particles in the case of the incubation time studies (Fig. 1a and Fig. 4a) and for three catalyst particles in the case of the 24 h incubation time studies (Fig. 1b) (Supplementary section 'Statistical analysis').

Catalytic testing and imaging. Catalytic testing was performed using 100 mg of catalyst bodies in a rectangular quartz, fixed-bed reactor (inner diameter of 6 mm × 3 mm) with a weight hourly space velocity (WHSV) of 8 h^{-1}. Before reaction, the reactor was heated at 500 °C under a N_2 flow for 2 h, and then cooled to 350 °C. A He flow with a methanol saturation of ~15% was introduced by flowing He as carrier gas through a saturator containing methanol at 20 °C. Online analysis of the reactant and reaction products was performed immediately using an Interscience Compact GC equipped with an Rtx-wax and Rtx-1 column in series and an Rtx-1, Rt-TCEP and Al_2O_3/Na_2SO_4 in series, both connected to a flame ionization detector (FID). Products were identified according to retention times, and confirmed using reference standards. Methanol conversion was calculated as $([MeOH_{in}] - [MeOH_{out}])/[MeOH_{in}]$, with hydrocarbon ($C_nH_m$) product yields calculated based on carbon atoms: $n[C_nH_m]/[MeOH_{in}]$. (See Supplementary Methods for a description of the imaging procedure.)

Data availability

All data supporting the findings of this study are available within the Article and its Supplementary Information, and/or from the corresponding authors upon reasonable request.

Received: 17 March 2018; Accepted: 24 September 2018;
Published online: 5 November 2018

References

1. Zaworotko, M. J. Materials science: designer pores made easy. *Nature* **451**, 410–411 (2008).
2. Davis, M. E. Ordered porous materials for emerging applications. *Nature* **417**, 813–821 (2002).
3. Kitagawa, S. Porous materials and the age of gas. *Angew. Chem. Int. Ed.* **54**, 10686–10687 (2015).
4. Serrano, D. P., Escola, J. M. & Pizarro, P. Synthesis strategies in the search for hierarchical zeolites. *Chem. Soc. Rev.* **42**, 4004–4035 (2013).
5. Cejka, J., Centi, G., Perez-Pariente, J., Roth, W. J. & Heyrovsk, J. Zeolite-based materials for novel catalytic applications: opportunities, perspectives and open problems. *Catal. Today* **179**, 2–15 (2011).
6. Parlett, C. M. A., Wilson, K. & Lee, A. F. Hierarchical porous materials: catalytic applications. *Chem. Soc. Rev.* **42**, 3876–3893 (2013).
7. Jones, A. C. et al. The correlation of pore morphology, interconnectivity and physical properties of 3D ceramic scaffolds with bone ingrowth. *Biomaterials.* **30**, 1440–1451 (2009).
8. Hollister, S. J. Porous scaffold design for tissue engineering. *Nat. Mater.* **4**, 518–524 (2005).
9. Pagliai, M., Vignozzi, N. & Pellegrini, S. Soil structure and the effect of management practices. *Soil Tillage Res.* **79**, 131–143 (2004).
10. Nair, B. N. et al. Synthesis of gas and vapor molecular sieving silica membranes and analysis of pore size and connectivity. *Langmuir* **16**, 4558–4562 (2000).
11. Moghaddam, S. et al. An inorganic–organic proton exchange membrane for fuel cells with a controlled nanoscale pore structure. *Nat. Nanotech.* **5**, 230–236 (2010).
12. Milina, M., Mitchell, S., Cooke, D., Crivelli, P. & Pérez-Ramírez, J. Impact of pore connectivity on the design of long-lived zeolite catalysts. *Angew. Chem. Int. Ed.* **54**, 1591–1594 (2015).
13. Du, J. et al. Hierarchically ordered macro- mesoporous TiO_2–graphene composite films: improved mass transfer, reduced charge recombination, and their enhanced photocatalytic activities. *ACS Nano.* **5**, 590–596 (2011).
14. Pérez-Ramírez, J., Christensen, C. H., Egeblad, K., Christensen, C. H. & Groen, J. C. Hierarchical zeolites: enhanced utilisation of microporous crystals in catalysis by advances in materials design. *Chem. Soc. Rev.* **37**, 2530–2542 (2008).
15. Hartmann, M. Hierarchical zeolites: a proven strategy to combine shape selectivity with efficient mass transport. *Angew. Chem. Int. Ed.* **43**, 5880–5882 (2004).
16. Christensen, C. H., Johannsen, K., Schmidt, I. & Christensen, C. H. Catalytic benzene alkylation over mesoporous zeolite single crystals: improving activity and selectivity with a new family of porous materials. *J. Am. Chem. Soc.* **125**, 13370–13371 (2003).
17. Mitchell, S., Michels, N.-L., Kunze, K. & Pérez-Ramírez, J. Visualization of hierarchically structured zeolite bodies from macro to nano length scales. *Nat. Chem.* **4**, 825–831 (2012).
18. Karwacki, L. et al. Morphology-dependent zeolite intergrowth structures leading to distinct internal and outer-surface molecular diffusion barriers. *Nat. Mater.* **8**, 959–965 (2009).
19. Fu, D. et al. Nanoscale infrared imaging of zeolites using photoinduced force microscopy. *Chem. Commun.* **53**, 13012–13014 (2017).
20. Ristanovic, Z., Kubarev, A. V., Hofkens, J., Roeffaers, M. B. J. & Weckhuysen, B. M. Single molecule nanospectroscopy visualizes proton-transfer processes within a zeolite crystal. *J. Am. Chem. Soc.* **138**, 13586–13596 (2016).
21. Zhu, X. et al. Probing the influence of SSZ-13 zeolite pore hierarchy in methanol-to-olefins catalysis by using nanometer accuracy by stochastic chemical reactions fluorescence microscopy and positron emission profiling. *ChemCatChem* **9**, 3470–3477 (2017).
22. Whiting, G. T. et al. Binder effects in SiO_2- and Al_2O_3-bound zeolite ZSM-5-based extrudates as studied by microspectroscopy. *ChemCatChem* **7**, 1312–1321 (2015).
23. Whiting, G. T. et al. Selective staining of Brønsted acidity in zeolite ZSM-5-based catalyst extrudates using thiophene as a probe. *Phys. Chem. Chem. Phys.* **16**, 21531–21542 (2014).
24. Mitchell, S., Michels, N.-L. & Pérez-Ramírez, J. From powder to technical body: the undervalued science of catalyst scale up. *Chem. Soc. Rev.* **42**, 6094–6112 (2013).
25. Corma, A., Grande, M., Fornés, V., Cartlidge, S. & Shatlock, M. P. Interaction of zeolite alumina with matrix silica in catalytic cracking catalysts. *Appl. Catal.* **66**, 45–57 (1990).
26. Corma, A., Martínez, C. & Sauvanaud, L. New materials as FCC active matrix components for maximizing diesel (light cycle oil, LCO) and minimizing its aromatic content. *Catal. Today* **127**, 3–16 (2007).
27. Corma, A., Grande, M., Fornés, V. & Cartlidge, S. Gas oil cracking at the zeolite–matrix interface. *Appl. Catal.* **66**, 247–255 (1990).
28. Corma, A., Martínez-Triguero, J. & Martínez, C. The use of ITQ-7 as a FCC zeolitic additive. *J. Catal.* **197**, 151–159 (2001).
29. Chen, N.-Y., Liu, M.-C., Yang, S.-C., Sheu, H.-S. & Chang, J.-R. Impacts of binder–zeolite interactions on the structure and surface properties of NaY–SiO_2 extrudates. *Ind. Eng. Chem. Res.* **54**, 8456–8468 (2015).
30. Yan T. Aromatization process and catalyst therefor. US patent 3,843,741A (1974).
31. Devadas, P., Kinage, A. K. & Choudhary, V. R. Effect of silica binder on acidity, catalytic activity and deactivation due to coking in propane aromatization over H-gallosilicate (MFI). *Stud. Surf. Sci. Catal.* **113**, 425–432 (1998).

32. Chowdhury, A. D. et al. Electrophilic aromatic substitution over zeolites generates Wheland-type reaction intermediates. *Nat. Catal.* **1**, 23–31 (2018).
33. Cychosz, K. A., Guillet-Nicolas, R., García-Martínez, J. & Thommes, M. Recent advances in the textural characterization of hierarchically structured nanoporous materials. *Chem. Soc. Rev.* **46**, 389–414 (2017).
34. Weinberger, C., Vetter, S., Tiemann, M. & Wagner, T. Assessment of the density of (meso)porous materials from standard volumetric physisorption data. *Micropor. Mesopor. Mater.* **223**, 53–57 (2016).
35. Xu, D., Ma, J., Song, A., Liu, Z. & Li, R. Availability and interconnectivity of pores in mesostructured ZSM-5 zeolites by the adsorption and diffusion of mesitylene. *Adsorption* **22**, 1083–1090 (2016).
36. Kenvin, J. et al. Quantifying the complex pore architecture of hierarchical faujasite zeolites and the impact on diffusion. *Adv. Funct. Mater.* **26**, 5621–5630 (2016).
37. da Silva, J. C. et al. Assessment of the 3D pore structure and individual components of preshaped catalyst bodies by X-ray imaging. *ChemCatChem* **7**, 413–416 (2015).
38. Liu, Y., Meirer, F., Krest, C. M., Webb, S. & Weckhuysen, B. M. Relating structure and composition with accessibility of a single catalyst particle using correlative 3-dimensional micro-spectroscopy. *Nat. Commun.* **7**, 12634 (2016).
39. Wei, Y., Parmentier, T. E., de Jong, K. P. & Zečević, J. Tailoring and visualizing the pore architecture of hierarchical zeolites. *Chem. Soc. Rev.* **44**, 7234–7261 (2015).
40. Zou, N. et al. Cooperative communication within and between single nanocrystals. *Nat. Chem.* **10**, 607–614 (2018).
41. Hendriks, F. C. et al. Single-molecule fluorescence microscopy reveals local diffusion coefficients in the pore network of an individual catalyst particle. *J. Am. Chem. Soc.* **139**, 13632–13635 (2017).
42. Hendriks, F. C. et al. Integrated transmission electron and single-molecule fluorescence microscopy correlates reactivity with ultrastructure in a single catalyst particle. *Angew. Chem. Int. Ed.* **57**, 257–261 (2018).
43. Conhaim, R. L. & Rodenkirch, L. A. Estimated functional diameter of alveolar septal microvessels in zone 1. *Am. J. Physiol. Heart Circ. Physiol.* **271**, H996–H1003 (1996).
44. Madden, C. J., Tupone, D., Cano, G. & Morrison, S. F. α2 Adrenergic receptor-mediated inhibition of thermogenesis. *J. Neurosci.* **33**, 2017–2028 (2013).
45. Soeller, C., Crossman, D., Gilbert, R. & Cannell, M. B. Analysis of ryanodine receptor clusters in rat and human cardiac myocytes. *Proc. Natl Acad. Sci. USA* **104**, 14958–14963 (2007).
46. Popielarski, S. R., Pun, S. H. & Davis, M. E. A nanoparticle-based model delivery system to guide the rational design of gene delivery to the liver. 1. Synthesis and characterization. *Bioconjugate Chem.* **16**, 1063–1070 (2005).
47. Fredrich, J. T., Menéndez & Wong, T.-F. Imaging the pore structure of geomaterials. *Science* **268**, 276–279 (1996).
48. Mauko, A., Muck, T., Mirtic, B., Mladenovic, A. & Kreft, M. Use of confocal laser scanning microscopy (CLSM) for the characterization of porosity in marble. *Mater. Charact.* **60**, 603–609 (2009).
49. Wang, W. Imaging the chemical activity of single nanoparticles with optical microscopy. *Chem. Soc. Rev.* **47**, 2485–2509 (2018).
50. Sperinck, S., Raiteri, P., Marks, N. & Wright, K. Dehydroxylation of kaolinite to metakaolin—a molecular dynamics study. *J. Mater. Chem.* **21**, 2118–2125 (2011).
51. Yarulina, I., Chowdhury, A. D., Meirer, F., Weckhuysen, B. M. & Gascon, J. Recent trends and fundamental insights in the methanol-to-hydrocarbons process. *Nat. Catal.* **1**, 398–411 (2018).
52. Keil, F. J. Methanol-to-hydrocarbons: process technology. *Micropor. Mesopor. Mater.* **29**, 49–66 (1999).
53. Buurmans, I. L. C. et al. Catalytic activity in individual cracking catalyst particles imaged throughout different life stages by selective staining. *Nat. Chem.* **3**, 862–867 (2011).
54. Qian, Q. et al. Single-particle spectroscopy on large SAPO-34 crystals at work: methanol-to-olefin versus ethanol-to-olefin processes. *Chem. Eur. J.* **19**, 11204–11215 (2013).
55. Palumbo, L. et al. Conversion of methanol to hydrocarbons: spectroscopic characterization of carbonaceous species formed over H-ZSM-5. *J. Phys. Chem. C* **112**, 9710–9716 (2008).
56. Van Speybroeck, V. et al. Mechanistic studies on chabazite-type methanol-to-olefin catalysts: Insights from time-resolved UV/vis microspectro scopy combined with theoretical simulations. *ChemCatChem* **5**, 173–184 (2013).
57. Mores, D., Kornatowski, J., Olsbye, U. & Weckhuysen, B. M. Coke formation during the methanol-to-olefin conversion: in situ microspectroscopy on individual H-ZSM-5 crystals with different Brønsted acidity. *Chem. Eur. J.* **17**, 2874–2884 (2011).
58. de Winter, D. A. M., Meirer, F. & Weckhuysen, B. M. FIB–SEM tomography probes the mesoscale pore space of an individual catalytic cracking particle. *ACS Catal.* **6**, 3158–3167 (2016).

Acknowledgements

The authors thank M. Rivera Torrente (Utrecht University, UU), I. Beurroies and M. V. Coulet (Aix-Marseille University) for Hg porosimetry data analysis, as well as R. Dalebout (UU) for Ar physisorption measurements. M. de Winter (UU) is thanked for his contribution to FIB–SEM measurements. F. Meirer (UU) and M. Vesely (UU) are also thanked for valuable discussions. This work was funded by a Netherlands Organisation for Scientific Research (NWO) Veni grant, awarded to G.T.W. (no. 722.015.003), a Marie Skłodowska-Curie grant agreement (no. 704544) (to A.D.C.) and a NWO Gravitation program (Netherlands Center for Multiscale Catalytic Energy Conversion, MCEC; to B.M.W.).

Author contributions

G.T.W., N.N., I.N. and A.D.C. contributed to the preparation, characterization and testing of samples. G.T.W. and B.M.W. designed and directed the project. All authors discussed the results and commented on the manuscript.

Competing interests

The authors declare no competing interests.

Additional information

Supplementary information is available for this paper at https://doi.org/10.1038/s41557-018-0163-z.

Reprints and permissions information is available at www.nature.com/reprints.

Correspondence and requests for materials should be addressed to G.T.W. or B.M.W.

Publisher's note: Springer Nature remains neutral with regard to jurisdictional claims in published maps and institutional affiliations.